

Programmable and Variable-Stiffness Robotic Skins for Pneumatic Actuation

Weinan Gao, Jingtian Kang, Guohui Wang, Haoxiang Ma, Xueyan Chen,*
Muamer Kadic, Vincent Laude, Huifeng Tan,* and Yifan Wang*

Pneumatic soft actuators possess relatively fast response, inherent high flexibility, and achieve extraordinary shape morphing under large deformations. Conventionally, the entire body of soft pneumatic robots needs to be designed for specific applications. Herein, a soft pneumatic actuator design with structured fabrics as actuator skins, which has high bending stiffness variation that can accomplish multiple tasks and different deformation modes in a single body, is proposed. By adjusting the structured skin, the developed soft actuator can be tailored to achieve various deformations. It is experimentally shown that the bending stiffness of the actuator can be adjusted from 108 to 5654 N m⁻¹. The blocking force of the actuator in bending is comparable with that of conventional fabric-reinforced pneumatic actuators, while the actuator skins are reusable and programmable. In application, the actuators are used to construct a bionic soft gripper with multiple degrees of freedom. By switching between three grasping modes, the gripper successfully fulfills a series of tasks including lifting weights up to 1 kg and grasping objects ranging from a grain of grape to a large iron basin. This work opens up an avenue for designing structured skins for pneumatic robots with programmable deformation modes and versatile functions.

the target in uncertain and dynamic environments,^[5–8] delicate manipulation and precise navigation of objects,^[9,10] and actuation with multiple degrees of freedom,^[11–15] that are not achievable with their rigid counterparts. These attributes lead to the demand for new generations of adaptive, reversible, and reconfigurable soft actuators. Soft actuators have been achieved with various mechanisms, including cables' tendon drive,^[16,17] electrical drive,^[18,19] pneumatical drive,^[20,21] etc. Among those possibilities, pneumatic pressure actuation is the most popular and low-cost means to exert forces and perform tasks with a soft body. The corresponding soft pneumatic actuator is also known as an elastic inflatable actuator (EIA).

Elastic inflatable actuation is generally facilitated by inflating a sealed elastomer chamber with controlled supply pressure. The chamber internal structure and outer surface is carefully designed to allow the


EIA to move or rotate along a prescribed path, such as bending,^[22,23] twisting,^[24] or extension/contraction.^[25] To date, a variety of structural configurations, for instance braided-sleeved,^[25] fiber-reinforced,^[26] or pleated,^[27] have been embedded into the EIA design. Once fabricated, however, the stiffness of the EIA is

1. Introduction

Recently, soft robots have attracted widespread interest due to their irreplaceable functionalities in engineering applications,^[1–4] including intrinsically safe interactions with

W. Gao, X. Chen, H. Tan
National Key Laboratory of Science and Technology on Advanced Composites in Special Environments
Harbin Institute of Technology
Harbin 150001, China
E-mail: chenxueyan@hit.edu.cn; tanhf@hit.edu.cn

W. Gao, J. Kang, G. Wang, Y. Wang
School of Mechanical and Aerospace Engineering
Nanyang Technological University
50 Nanyang Avenue, Singapore 639798, Singapore
E-mail: yifan.wang@ntu.edu.sg

 The ORCID identification number(s) for the author(s) of this article can be found under <https://doi.org/10.1002/aisy.202300285>.

© 2023 The Authors. Advanced Intelligent Systems published by Wiley-VCH GmbH. This is an open access article under the terms of the Creative Commons Attribution License, which permits use, distribution and reproduction in any medium, provided the original work is properly cited.

DOI: 10.1002/aisy.202300285

J. Kang
Key Laboratory of Structural Dynamics of Liaoning Province
College of Sciences
Northeastern University
Shenyang 110819, P. R. China

H. Ma
Deep Sea Engineering Division
Institute of Deep Sea Science and Engineering
Chinese Academy of Sciences
Sanya, Hainan 572000, China

M. Kadic, V. Laude
Institut FEMTO-ST
CNRS
Université Bourgogne Franche-Comté
25030 Besançon, France

usually fixed, and the deformation mode of the EIA only follows the predesigned path. Consequently, pneumatic soft robots can only perform one or a small number of tasks in a minimal range. In the future, it is likely that robots will be required to change tasks regularly, setting stronger requirements on stiffness variability and deformation mode reconfigurability.^[16,28] Moreover, robots may need to provide adaptable bending stiffness and force to different target objects with different surface pressure endurance, particularly for soft and heavy objects. Therefore, it is imperative to develop a highly versatile and adaptable EIA with tunable mechanical properties.

Structured fabrics, such as woven sheets and chain-mail structures, typically show high conformability and shape adaptability which result from their intrinsically soft constitutive material or interlocking structural configuration.^[29–32] A recent study has revealed that the stiffness of chain-mail-based structured fabrics manufactured by selective laser sintering 3D printing could be adjusted by application of a magnetic field.^[33] Moreover, structured fabric, consisting of 3D particles arranged into layered chain mails, can make use of the principle of the jamming phase transition to achieve a tunable bending modulus.^[31] When exerting a pressure on the boundaries of the chain-mails, the adjacent particles would jam and switch from a soft to a rigid state. Chain-mail-based fabrics with tunable mechanical properties undoubtedly provide routes toward lightweight, tunable, and adaptive soft robots, with potential applications to wearable exoskeletons,^[34,35] haptic architectures, and reconfigurable medical supports. However, it still remains a big challenge to tailor the bending mode of soft robots.

Here, we demonstrate a new method to design a pneumatic tubular actuator with tunable bending modulus and the capacity to accomplish multiple tasks with various deformation modes, enabled by the integration of elastic pneumatic chambers and wearable 3D structured fabrics. Unlike the conventional EIA, the actuator skin composed of structured fabrics can be easily adjusted and replaced when required. Accordingly, the elastomer tube can be actuated in the selected path tailored by the skin. As an example, we demonstrate that the elastomer tube can be made to bend in any direction by rotating the orientation of the structured skin. This mechanism is further extended to construct a bionic pneumatic soft gripper. The gripper with multiple degrees of freedom can position items within ample working space. By switching between three grasping modes, the gripper successfully fulfills a series of tasks with weights up to 1 kg and shapes ranging from a small grain of grape to a large iron basin.

2. Results

2.1. Design of the Pneumatic Tubular Actuator with Structured Fabrics as Skin

We first outline the general design procedure for combining the advantages of elastic tubes and structured fabrics in view of achieving tailored bending deformation. As illustrated in **Figure 1**, the proposed soft pneumatic actuator consists of an elastomeric air tube inserted in a structured skin. Several pieces of structured fabrics of different unit cell dimensions are stitched together to form the structured skin. As the elastomeric tube is confined within the asymmetric structured skin, it deforms

nonuniformly when inflated. Since the tube and the structured skins are disjoint, the deformation modes can be easily customized by redesigning the structured skin.

As illustrated in **Figure 1A**, resembling ancient chain-mail armor,^[30] the structured fabric is composed of linked hollow octahedral unit cells with identical geometrical features oriented in different directions. By rotating the central blue octahedron by 45° around the z-axis, the adjacent vertical octahedral structures marked in yellow are obtained. Similarly, the adjacent horizontal element is generated when the central octahedron is rotated along the y-axis by 45°. The elements mentioned above are linked together periodically to form the structured fabric, which can be fabricated by 3D printing technology. When applying a biaxial stretch, the structured fabric expands and the geometrical constraints of the gaps confine and steer the expansion.

The elastomeric tube is made of silicon rubber and has a direction knob and an inflation plug, as shown in **Figure 1B**. During curing, the plastic plug is perfectly fixed to the elastomeric tube. It connects the air tube used for inflation with the elastomeric tube. The direction knob can rotate around the inflation plug without a translational displacement. In the following, the structured fabrics are directly attached to the direction knob rather than to the elastomeric tube. Thus, the relative angle between the structured fabric and the elastomeric tube can be controlled by rotating the direction knob. When inflating, the free elastomeric tube expands as a balloon without bending, as shown in **Figure 1B**.

The structured skin is composed of several pieces of structured fabrics with different unit cell designs. For instance, **Figure 1C** illustrates a structured skin created by combining two structured fabrics with hollow octahedrons of different sizes. The structured fabric with the larger unit cell length l (see **Figure 1A**) is named Structure A, whereas the other is named Structure B. Consequently, compared to Structure A, Structure B has shorter gaps, which are the maximum distances between the vertex pairs, such as D_{12} and D_{34} illustrated in **Figure 1A**. Much like tailors, we flip, align, and stitch the flat structured fabrics together to form a structured skin (for details, please see Supporting Information). After putting on the structured skin, the elastomeric tube becomes an elastic pneumatic actuator, as shown in **Figure 1D**. Initially, the tubular actuator remains straight. After inflation, the bending angle increases with the air pressure, and the tubular actuator remains stable at the designed angle. **Figure 1D** shows that the tubular actuator always bends toward the side of the smaller octahedrons. As a whole, the elastomeric tube provides a driving force upon inflating, whereas the structured skin governs the deformation of the tubular actuator.

2.2. Variable-Stiffness Measurement of the Pneumatic Tubular Actuator

To investigate the change in bending stiffness, we conducted a three-point bending test in the particular case where hollow octahedrons all have the same size (the skin is composed of a single piece of fabric). The force–displacement curves when internal air pressure, P , in the actuator ranges from 0 kPa to 100 kPa are obtained and shown in **Figure 2A**. As pressure increases, the force applied on the test piece gradually increases for the same applied displacement. Its variation is almost linear, which

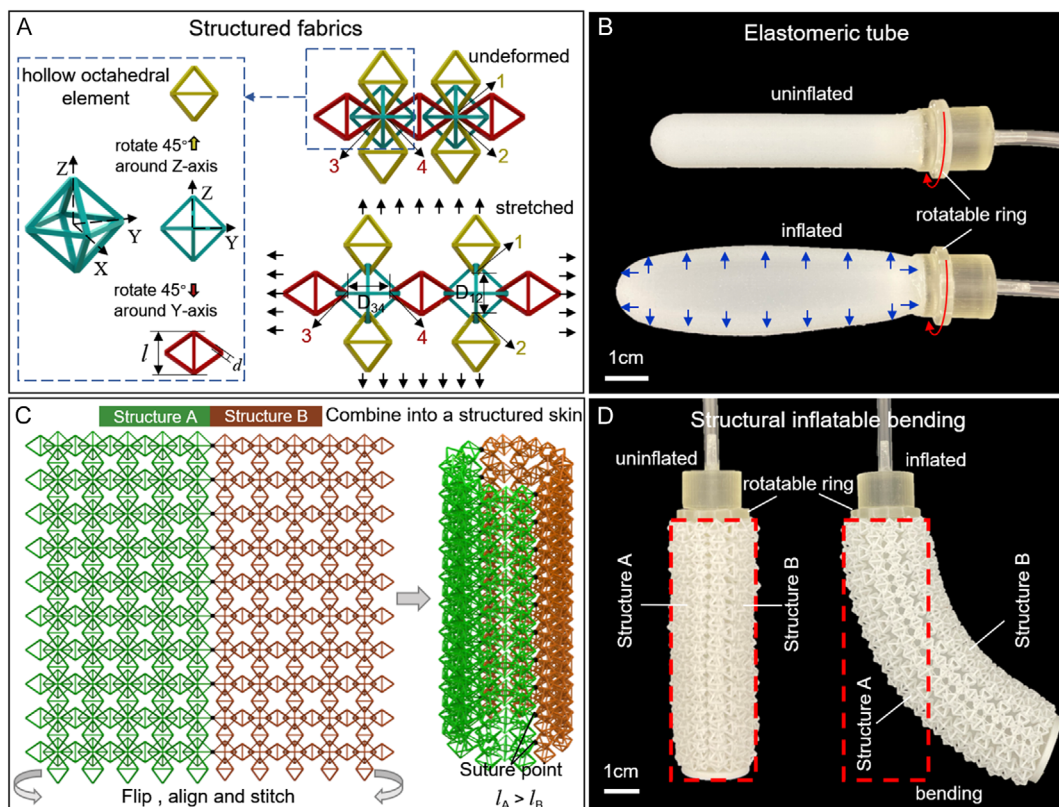


Figure 1. General process for designing and assembling the soft pneumatic actuator. A) The composition of the chain-mail structured fabric is depicted. B) Unlike classical pneumatic actuators with multiple pneumatic channels, the design includes only one elastomeric tube that expands like a balloon when inflated. C) Two pieces of structured fabrics with different octahedral sizes are used to induce inhomogeneous stiffness. In contrast to Structure A ($l_A=8$ mm, $d=0.5$ mm), Structure B ($l_B=6.5$ mm, $d=0.5$ mm) that has a smaller effective length is more rigid, thanks to the shorter distance between intersection points. The two parts are flipped and stitched to form a tubular structured fabric skin. D) Photographs of the original and deformed frames of the experimental sample are shown.

indicates that the proposed pneumatic actuator has a stable bending resistance. When the displacement reaches 5 mm, the maximum force on the test piece is 0.50 N for an internal pressure of 0 kPa, whereas it is 28.13 N for an internal pressure of 100 kPa, almost 56 times larger. These mechanical properties make it a potential candidate for loading bearing and robot application. To further support this point, Figure 2B displays the bending stiffness as air pressure varies. Bending stiffness, a crucial characteristic of the soft pneumatic actuator, is defined as the ratio of the reacting force to air pressure. It is observed that the bending stiffness scales nonlinearly with air pressure. For the range $P \in [0:100]$, one can easily adjust the bending stiffness from 108 to 5654 N m^{-1} according to the fitting function illustrated in Figure 2B. As a result, the proposed elastic actuator possesses remarkable capacity for tailoring bending stiffness.

2.3. Bending of Structured Fabrics

Bending is the most common deformation mode of a pneumatic tubular actuator and is widely used in soft robotics. The bending deformation of the proposed elastic actuator is mainly enabled by the structured skin. In order to understand the deformation mechanism, a structured fabric with two types of hollow

octahedrons is first investigated. The undeformed state of Structures A (green) and B (brown) is shown in Figure 3A. The structured fabric is geometrically described by the following six independent parameters: the rod diameter of the hollow octahedrons d , the unit cell lengths of structures A and B, l_A and l_B , the column numbers of structures A and B, n_1 and n_2 , and the number of rows of the structured fabrics m . There are some inherent geometrical constraints that apply to the structured fabric. $m \geq 2$ is a premise for the occurrence of a bending angle. To stitch two pieces of structured fabrics with different sizes together, it is required that l_B should be within a range determined by l_A and d

$$\frac{l_A}{2} + d \leq l_B \leq 2(l_A - d) \quad (1)$$

We define b_1 and b_2 as the distances between neighboring rows of structured fabrics with large and small sizes, respectively. Based on the characteristics of the linked structure, b_1 and b_2 , which change with rigid motion, are geometrically confined by relations

$$\sqrt{2}l_A \leq b_1 \leq 2\sqrt{2}(l_A - d) \quad (2)$$

and

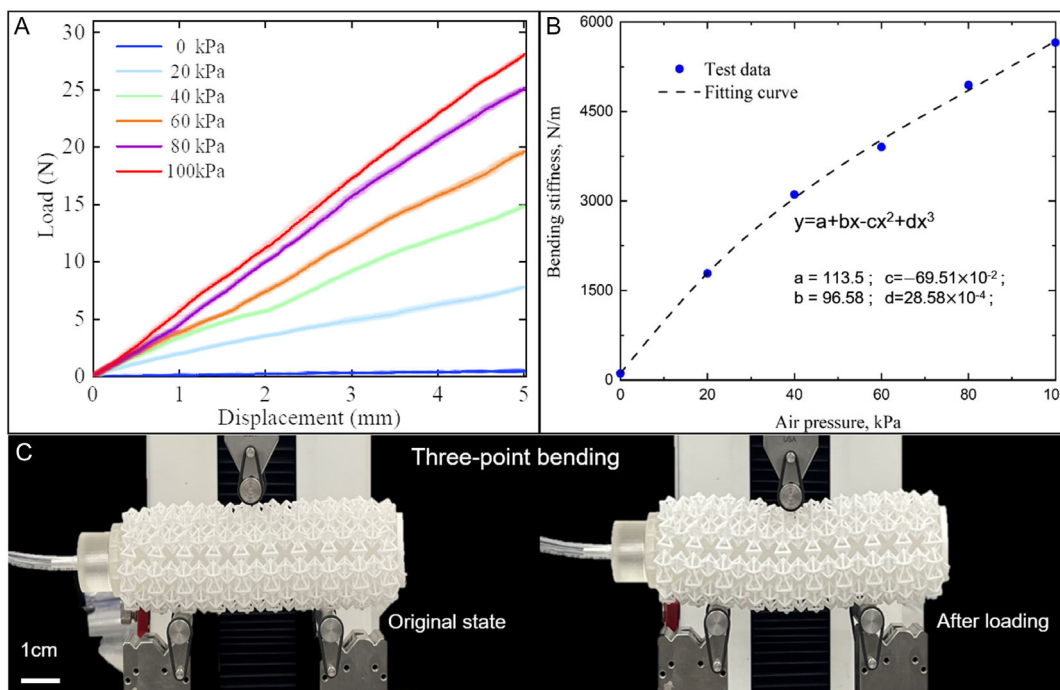


Figure 2. Three-point bending test of the soft pneumatic actuator. A) The force–displacement curves of the elastic pneumatic actuator under different air pressures are mostly linear. B) Evolution of the bending stiffness of the pneumatic actuator as a function of air pressure obtained by experimental test and curve fitting. C) Photographs of the corresponding deformation frames are shown before and at the maximum of the three-point bending test.

$$\sqrt{2}l_B \leq b_2 \leq 2\sqrt{2}(l_B - d) \quad (3)$$

B is defined as the distance from the center of the left octahedra to the center of the right octahedra (see Figure 3A). This distance must be within the range

$$\frac{\sqrt{2}}{2}(l_A + l_B) + \sqrt{2}[(n_1 - 1)l_A + (n_2 - 1)l_B] \leq B \leq \frac{\sqrt{2}}{2}(l_A + l_B) + 2\sqrt{2}[(n_1 - 1)(l_A - d) + (n_2 - 1)(l_B - d)] \quad (4)$$

Initially, the octahedra in the structured skin are lumped together. There are no gaps available between neighboring octahedra. The values of b_1 , b_2 , and B assume the lower bounds of the inequalities in Equation 2–4. Under stretching, the distance between neighboring rows and columns increases until the upper bound is reached. Rotation occurs when Structure B reaches its limit whereas Structure A still has not. The rotation angle of the structured fabric can be estimated by

$$\theta = 2(m - 1)\arcsin \frac{b_1 - b_2}{2B} \quad (5)$$

Substituting the extreme values for b_1 , b_2 , and B into Equation (5), the maximum bending angle can be expressed as

$$\theta_{\max} = 2(m - 1)\arcsin \frac{2\left(1 - \frac{l_B}{l_A}\right)}{\left(1 + \frac{l_B}{l_A}\right) + 4\left[(n_1 - 1)\left(1 - \frac{d}{l_A}\right) + (n_2 - 1)\left(\frac{l_B}{l_A} - \frac{d}{l_A}\right)\right]} \quad (6)$$

To verify the above derivation, a uniaxial tensile test was conducted with the structured fabric (see Figure 3B). The sample features a rod diameter $d = 0.5$ mm, and unit cell lengths $l_A = 8$ mm and $l_B = 6.5$ mm. The row and column numbers for each part are 8 and 2, respectively. The structured fabric sheet is fixed on two flat plates. We drill holes in the middle of each plate, through which fishing lines are used to stretch the robotic skin sheet. A tensile force of 10 N is applied to observe the deformation of the test sample. A special fixture configuration was adopted to allow the structured skin to bend freely in the plane. Once stretched, the sample would suffer from an initial uniform deformation phase. It followed a steady rotational deformation resulting from structural asymmetry. The rotational deformation would continue until particles in structure A attained their geometrical limit. By then, the ultimate configuration and the maximum bending angle are attained. Subsequently, plastic deformation occurred and prevailed. The maximum bending angle measured by the relative rotation between the top and bottom acrylate plates was 34.4° . This process was also numerically simulated for verification using the commercial finite element software ABAQUS with an Explicit FE solver (see Figure S2 and Movie S1, Supporting Information for detailed results). The maximum bending angles predicted by the numerical solver and by Equation (6) were 36.2° and

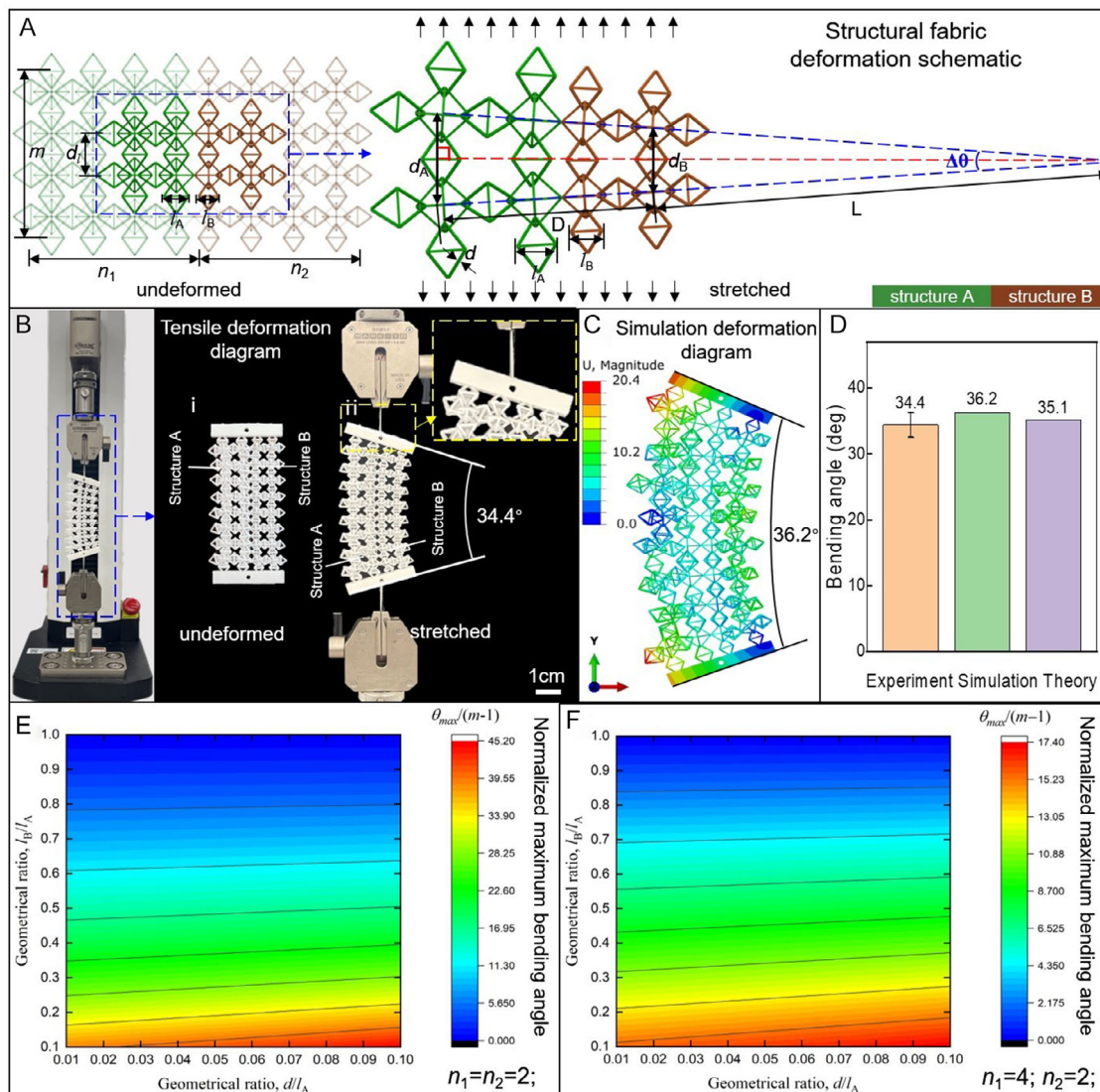


Figure 3. Bending mechanism of the structured fabric sheet. A) A schematic diagram is shown for the deformation of the structured fabrics upon stretching. The structured fabrics are sewn from octahedra of different sizes that bend under tension, with the maximum global bending angle of the structured fabric being ruled by geometrical dimensions. B) A uniaxial tensile test on the structured fabric sheet was conducted to validate the bending behavior and to measure the maximum bending angle. C) The deformation frame and the corresponding maximum bending angle of the structured fabrics are obtained from numerical simulation. D) A comparison of the maximum bending angles predicted by experiment, simulation, and theory is proposed. E, F) Contour plots illustrate the dependency with geometrical ratios of the maximum bending angle of the structured fabric, for column numbers $n_1 = 2$, $n_2 = 2$ (E) and $n_1 = 4$, $n_2 = 2$ (F).

35.1°, both of them being very close to the result of the test. The good agreement between theory, simulation, and experiment validates the design. The evolution of the normalized maximum bending angle is illustrated in Figure 3 as a function of the geometrical ratios l_B/l_A and d/l_A . When the numbers of columns n_1 and n_2 equal 2, the normalized maximum bending angle increases with l_B/l_A and d/l_A . Note that the normalized maximum bending angle vanishes when l_A is equal to l_B . A similar trend is found in Figure 3F that further indicates that the bending effect is suppressed when the number of columns increases.

2.4. Bending of the Pneumatic Tubular Actuator Guided by Structured Skins

After identifying the underlying bending mechanism of structured fabrics, the effect of skin structure on the elastic response of the tubular actuator is investigated. Cylindrical structured skins are fabricated by rolling and stitching together two pieces of structured fabrics of different sizes (see Figure 1C). The cylindrical structured skin is geometrically controlled by the same parameters as the structured fabric sheet discussed above. The definition of geometrical parameters remains unchanged except

for distance B . In cylindrical structured skin, B refers to the diameter of its circular cross section (see Figure S1, Supporting Information), which certainly varies with circumference stretching within a range. The numbers of columns for Structure A and Structure B are selected to be the same; hence, $n_1 = n_2$. Adopting a method of analysis similar to the case of the structured fabric sheet, the maximum bending angle induced by the tubular robotic skin is

$$\theta_{\max} = 2(m - 1) \arcsin \frac{\pi \left(1 - \frac{l_B}{l_A}\right)}{\left(1 + \frac{l_B}{l_A}\right) + 2(n_1 - 1) \left[\left(1 - \frac{d}{l_A}\right) + \left(\frac{l_B}{l_A} - \frac{d}{l_A}\right)\right]} \quad (7)$$

To understand better the deformation of the tubular actuator, we fabricated an elastic pneumatic actuator and characterized its bending behavior. Two different structured skins were considered to investigate the influence of geometrical parameters on bending. For both configurations, the numbers of columns and rows of hollow octahedra were chosen equal in Structures A and B ($m=13$, $n_1=n_2=6$). Configuration 1 is composed of an elastic tube and octahedra with relatively large dimensions ($l_A=8$ mm, $l_B=6.5$ mm), whereas configuration 2 is composed of smaller octahedra ($l_A=6.5$ mm, $l_B=5$ mm). Here, we take configuration 1 as an example to introduce the general deformation rule.

In the experiment, it is observed that the tubular actuator always bends toward the side with smaller octahedra, hence structure B (see Movie S2). According to the deformation characteristics, the bending process can roughly be divided into three successive stages. Once inflated, the actuator responds quickly and enters the first stage. In this stage, the pneumatic tubular actuator slightly expands in length. The second stage occurs after the gaps of structure B have attained their maximum. At the moment, there is still enough space left for structure A to expand. Consequently, the tubular actuator bends toward structure B. The bending angle increases with the pressure until the gaps of structure A unfold entirely. In the last stage, the bending angle remains almost unchanged during inflation, while the tension between neighboring octahedra increases rapidly. Further increasing the inner pressure triggers plastic deformation of the structured skin, which is crucial to increase the actuator stiffness and support the bending moment.

Figure 4A illustrates the terminal state of the tubular pneumatic actuator in the inflating experiment (Details of the Experimental Section are summarized in Figure S3, Supporting Information). The measured bending angle is about 46.3° . The deformation of the tubular actuator obtained from numerical simulation is plotted in Figure 4B. The estimated bending angle is 44.6° . The good agreement between simulation and experiment validates the design. The relationship between bending angle and air pressure for configurations 1 and 2 is depicted in Figure 4C. The variations of the bending angle obtained from numerical simulations are in line with experiments (see also Movie S2, Supporting Information). The maximum bending angles are successfully predicted by Equation (7). The bending angle for configuration 2 is always larger than that for configuration 1 under the same pressure and almost reaches

58.1° . Note that the first stage of the bending process is not apparent in Figure 4C. This may be attributed to the fact that the extension does not dominate the deformation of the pneumatic tubular actuator. Moreover, in order to reduce experimental dispersion, we applied pretension on the structured skin, which further limits the linear expansion range.

To some extent, the bending angle decides the size and shape of an item that the soft robot can grasp, and the output force determines how firmly that item can be grasped. We then explore experimentally the output force in Figure 4D. More details regarding the experimental setup (see Figure S3A,B, Supporting Information) and the characterization method are presented in the supplementary material. It is clear that the output forces almost linearly increase with the applied pressure. Unlike the bending angle, the geometrical ratio has a limited effect on the output forces. The output force generated by configuration 2 is slightly larger than the one generated by configuration 1. When the applied pressure is 100 kPa, the corresponding maximum output force of configuration 2 is almost 6.81 N, which is comparable with other fiber-reinforced pneumatics actuators.^[28,36]

Next, we examine experimentally the effect of the sectional ratio on the performance of the pneumatic actuator. The sectional ratio is defined as the area occupied by structure A divided by the total area. By definition, the sectional ratio ranges from 0 to 1. For configuration 1, when the sectional ratio equals 0 or 1, the structured skin only contains 6.5 mm or 8 mm octahedra. In either case, the structured skin has a homogeneous distribution. The pneumatic actuator tends to expand rather than to bend. Figure 4E illustrates the influence of the sectional ratio on the bending of the tubular actuator. For all sectional ratios, the bending angle curves exhibit similar trends. When the sectional ratio has symmetrical values, such as $1/6$ and $5/6$, $1/3$, and $2/3$, the proportions of large and small structure fabrics are interchanged. In comparison, configuration 1 with a sectional ratio of $5/6$ or $2/3$ performs better than that with smaller sectional ratios. Structure A dominates the bending behavior. When the sectional ratio is $1/2$, the bending angle is maximum. This is attributed to the fact that bending is fully activated when the aspect ratio is farther away from 0 and 1. Similarly, the output force is also maximum when the sectional ratio is $1/2$ (see Figure 4F). For most sectional ratios, the output force is approximately linear with the applied force. When the sectional ratio is $1/6$, the output force is significantly less than for other configurations. It may be because an inappropriate proportion introduces too many small-sized octahedra, thereby blocking the bending deformation.

2.5. Multiple Deformation Modes and Reusability of the Pneumatic Tubular Actuator

For conventional pneumatic actuators, the bending direction is fixed once the multiple air channels are cured. If one intends to adjust the bending direction, the air channel or the fixture must be redesigned to ensure the targeted inflating sequence. To overcome this difficulty, the structured skin attached to a knob is made independent of the elastomeric tube. By rotating the knob, the bending direction of the tubular actuator can be altered to any

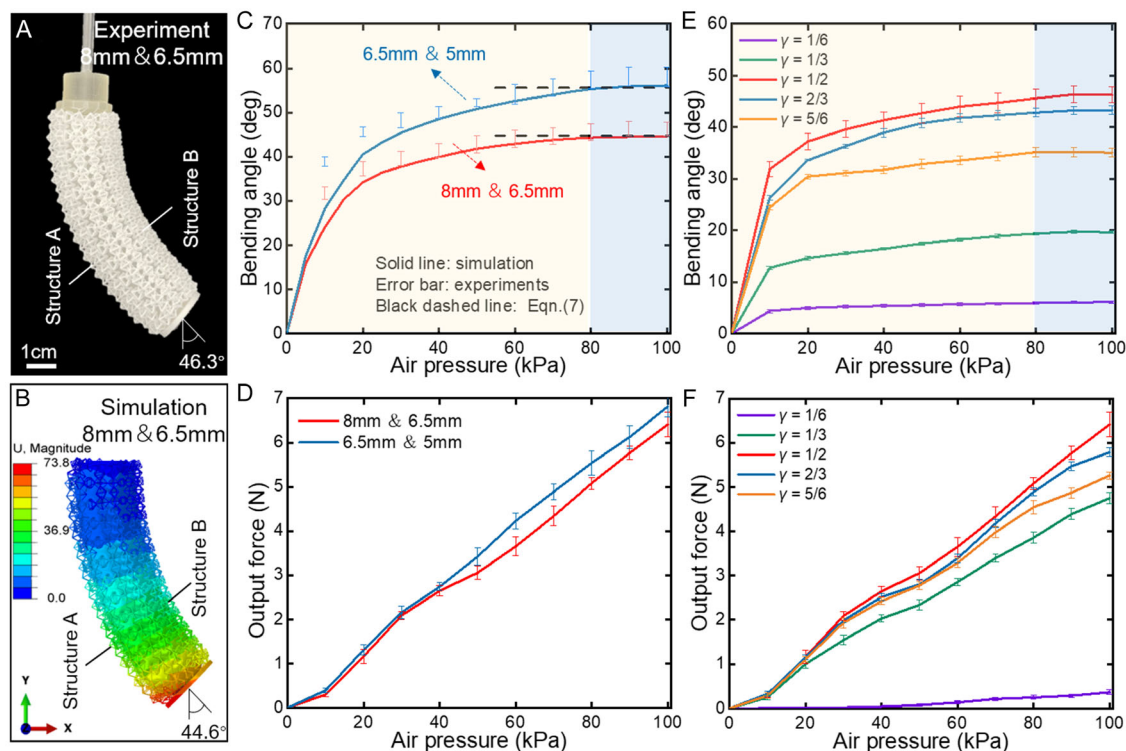


Figure 4. Bending of the tubular actuator in response to the applied pressure. A) A photograph of the terminal stage of configuration 1 in the inflation experiment is shown. B) The deformation frame and the bending angle of the tubular actuator were obtained from the numerical simulation. C) The bending angle versus air pressure is shown for both configurations (8 mm & 6.5 mm and 6.5 mm & 5 mm). Solid lines and error bars are from simulations and experiments, respectively. The dashed line indicates the result from Equation (7). D) The output forces for both configurations are plotted as a function of air pressure. E) The bending angle and F) the output force are obtained experimentally as a function of the sectional ratio γ and the air pressure.

angle, such as 45, 90, 180, and 315°, even if it is in working condition (see **Figure 5A** and **Movie S3**, Supporting Information).

Apart from bending deformation, the structured skin enables the pneumatic tubular actuator to present other deformation modes by altering the distribution of the structured fabrics. For instance, S-shape bending can be achieved by rearranging the structured fabrics from symmetric to antisymmetric (in the up-and-down direction), as shown in **Figure 5Bi,ii**. Similarly, an inflated gourd-shape configuration can be designed by adopting the same structured fabrics with bilateral symmetrical distribution, as illustrated in **Figure 5Bii,iii**. If we entirely remove the small-size or large-size octahedra, the pneumatic tubular actuator will only generate an extensional deformation, as shown in **Figure 5Biv**. These variable deformation modes make it feasible to achieve complicated movement and multiple functions.

Significantly, one advantage of the proposed structured skins is their reusability. Two different kinds of skins, 8 mm & 6.5 mm and 6.5 mm & 5 mm, were considered here to assemble pneumatic actuators for the following inflation and deflation cycling experiment (see **Movie S3**, Supporting Information). **Figure S5**, Supporting Information, shows the test data of 30 cycling loading experiments for both configurations. It is clear that both actuators possess almost constant output bending angles of about 58.08° and 46.03° with the same input air pressure of 80 kPa.

Good repeatability validates the reusability of pneumatic actuators. Additionally, a structured skin can be recycled by a simple tailoring procedure to make a new skin, as illustrated in **Figure 5C**. For the assembly of structured skins, different pieces of fabric are stitched together along seams. It is easy to remove certain stitched points and to separate structured fabrics apart. The separated structured fabrics can be rearranged into new positions by rotations and translations, before stitching them together to generate a new structured skin. The dominated deformation behavior can then transform from a bending mode to a gourd-shape mode (see **Figure 5B i,iii**). The whole process should only take a couple of minutes. Moreover, there is no need to reprint the soft skin, which makes the proposed structured skin more durable in light of economic and environmental considerations.

2.6. Manipulation by the Soft Pneumatic Gripper

We further demonstrate the possibility of utilizing the proposed tubular actuator to construct a soft gripper. Here, the soft gripper is composed of an arm, three fingers, and an attached 3D-printed triangular frame (see **Figure 6A**). The accessible working space is generally decided by the length and the bending angle of the soft arm, whereas grasping movements are mainly controlled by the

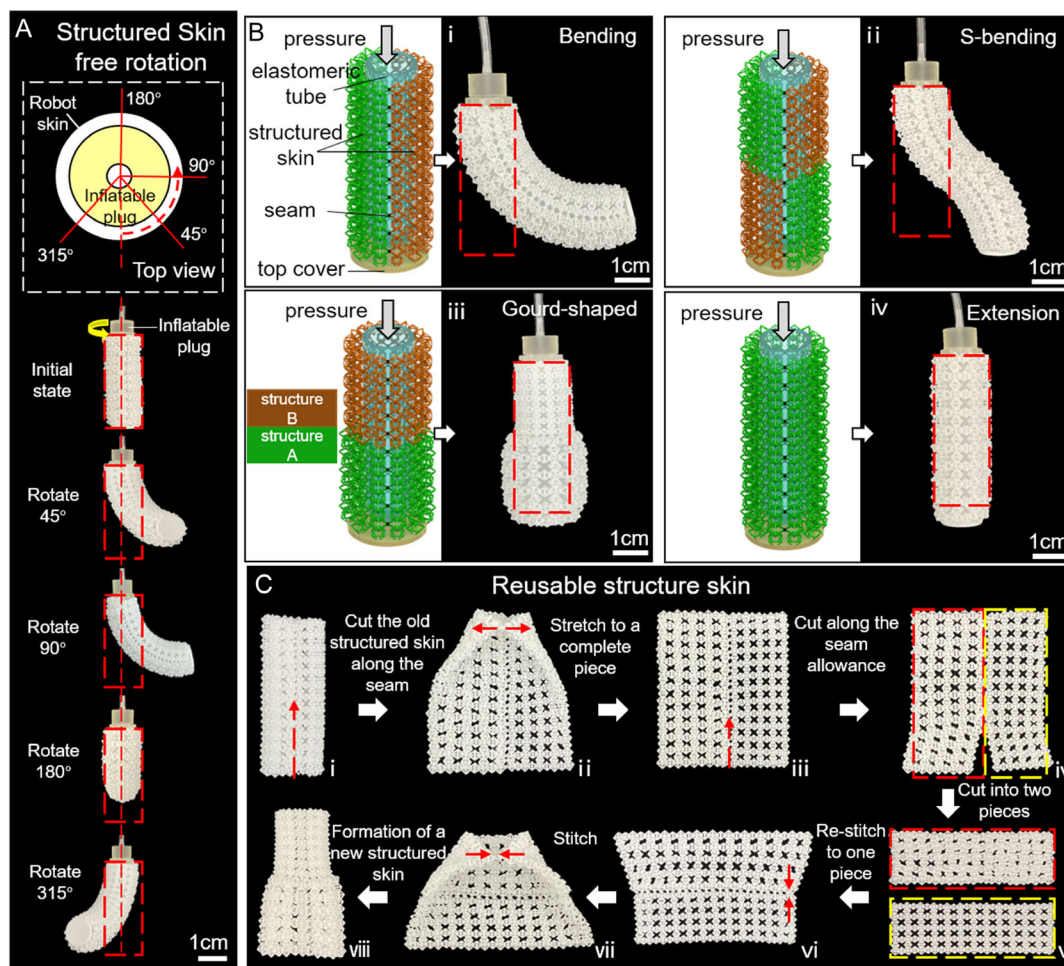


Figure 5. Multiple deformation modes and reusability of the tubular actuator. A) The separated design of the structured skin and the elastomeric tube enables us to adjust the bending direction of the tube to any desired direction without taking off the fixture. B) By altering the structured skin, the tubular actuator can be adjusted to diverse deformation forms: i) bending; ii) S-shaped bending; iii) gourd-shaped bending; and iv) extension. C) A general process to recycle the old structured skin and generate a new one with a new deformation mode: i) remove the stitching points; ii) flatten the skin; iii–v) split the skin; and vi–viii) rearrange structures A and B and stitch them together again to generate the new configuration (iii, iv).

collaboration of the soft fingers. For these requirements to hold, each configuration needs to be controlled by separate air channels. Fingers are connected in series, ensuring that all fingers have the same internal pressure and output force at the fingertips when grasping objects. Configuration 2 considered above is used for the soft fingers. Considering the working space and the supporting capacity, the tubular actuator used for the soft arm must be more extended and robust. Herein, the soft arm is about 1.78 times as long and 1.81 times as wide as the soft fingers. Its attaching structured skin is adjusted accordingly. The number of rows m and the number of columns n_1 and n_2 are changed to 23 and 11, respectively. More details can be found in Supporting Information (Figure S3 and Table S1, Supporting Information).

Benefiting from its reusable and multimodal structured skin, the proposed soft gripper can be tailored to various postures. Figure 6B illustrates three typical working modes that mimic the human hand: pinching, stretching, and holding. These working modes are all accomplished by pumping air into the

elastomeric tubes. They can be transformed between each other by rotating the structured skin toward the desired directions (see Movies S4 and S5). Aided by these working modes, the soft gripper can locate, grasp, lift, and move items with a wide range of shape, stiffness, and weight. For instance, we successfully realized object manipulation by pumping air into the soft arm, locating a milk bottle, operating the finger tubes to grasp the bottle, and finally releasing it (see Figure 6C and Movies S6 and S7, Supporting Information). The soft gripper can grasp not only a heavy and stiff milk bottle (803 g, Figure 6C), but also a light and flexible balloon (1 g, Figure 6D) in a gentle manner. The pinching mode can be used to grasp items with different shapes, as small as a grain of grape (Figure 6E) and as large as a round orange fruit (Figure 6F) or a slender banana (Figure 6G). The stretching mode is utilized to hold and move massive objects such as an iron basin (702 g, Figure 6H). Note that the weight is not the unique indicator for a soft gripper, the ability to adapt to the geometrical shape and structural flexibility of the object is equally important. It means that the gripper should provide

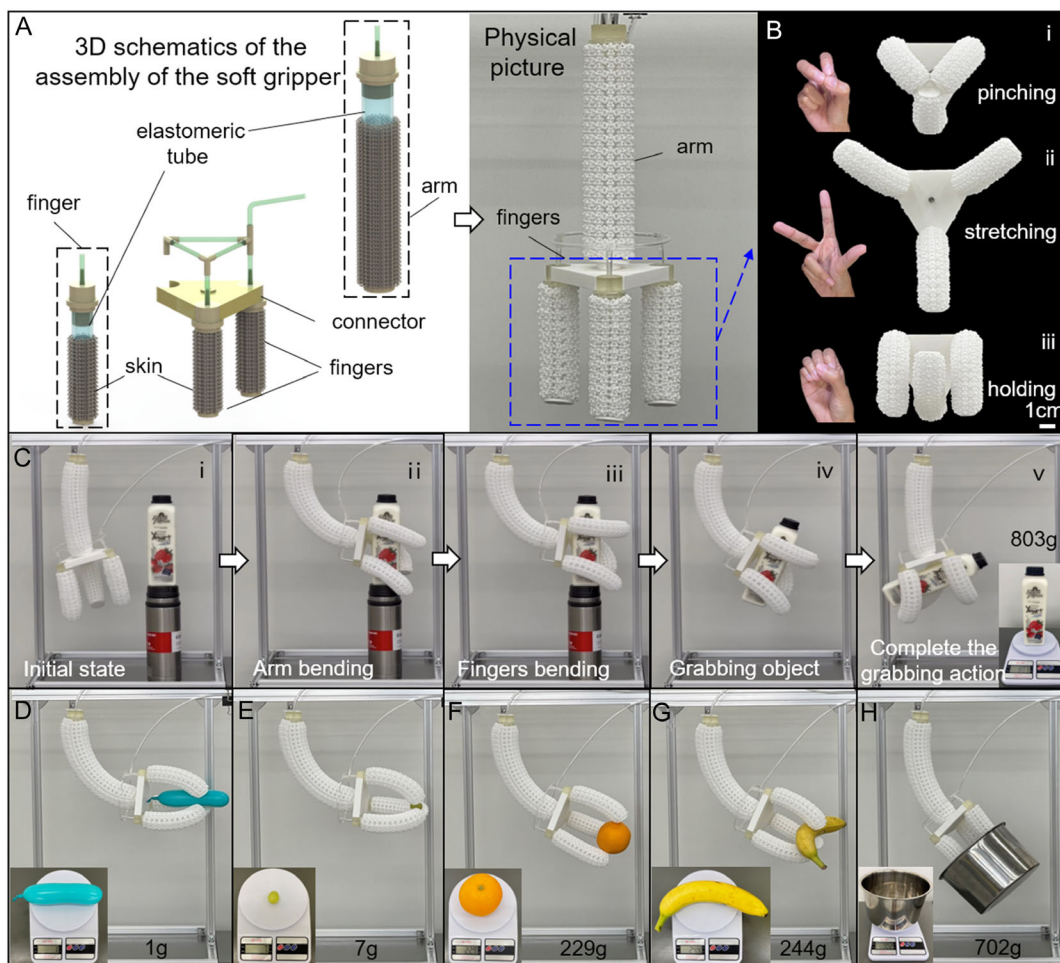


Figure 6. Pneumatic tubular gripper for soft robot application. A) The 3D assembly schematics and the physical picture of the soft gripper are shown. The arm is used for locating items and the fingers are used to grasp the movement. B) Three typical working modes for mimicking the human hand: pinching, stretching, and holding. C) A bottle of milk was taken as an example to introduce how to grasp and move a held target. With the aid of the pinching and the stretching modes, the soft gripper can also be used to manipulate objects with diverse shapes and weights: D) a light balloon of 1 g, E) a small grain of grape of 7 g, F) an orange fruit of 229 g, G) a long banana of 224 g, and H) a hollow iron basin of 702 g.

adaptable stiffnesses for different targets together with force. This rule can also explain the grasping operation. It is apparent the gripper cannot grasp objects without stiffness. Low stiffness is usually used to deal with objects with soft surfaces. For grapes and balloons, using a higher stiffness will lead to an unexpected out-of-plane deformation or even destroy the targeted object. Medium stiffness is more suitable for objects with a certain weight, size, and structural stiffness, such as bananas, oranges, and other fruits. One can adjust the stiffness and force accordingly. High stiffness is adopted to ensure the grasp quality for objects with high structural stiffness and a large amount of weight, such as stainless steel and rigid plastics products.

As a supplement, we have conducted another grasping experiment on a water balloon. The water balloon with a weight of up to 547.5 g is a typical soft but heavy object (see Figure S9, Supporting Information). From Movie. S9, it can be observed that the gripper could lift the water balloon very gently without hurting the target object. To further support this viewpoint, we conducted an additional grasping experiment on the water

balloon. As depicted in Figure S10, Supporting Information, the gripper begins in a relaxed state with the internal pressure set to 14 kPa. This ensures the gripper has low stiffness, enabling it to conform to the face of the water balloon. To eliminate the influence of the grasping force, we then meticulously modulate the internal pressure, but only within a narrow range. In this case, the pressure gauge continues to display a reading of 14 kPa. However, the bending stiffness of the gripper significantly varies to precisely conform to the surface features of the target object. Then, the gripper holds the water balloon in a tight state. Due to the characteristics of the interlocking structure, the structured fabric is very sensitive to air pressure and generally possesses a multistable state compared with other fixtures. These stable states play a critical role in determining the bending stiffness. Combined with the previous grasping experiment, it may conclude that the proposed soft gripper provides suitable bending stiffness to different target objects. As illustrated in Table S1, Supporting Information, the soft gripper can work within a circular space with a radius of 0.6 m. The soft fingers

mimicking the human hand have an open span of 305 mm. The grasping weight ranges from 1 g to about 1000 g using the different grasping modes.

3. Conclusion

Here, we presented a novel way to design and fabricate a class of soft pneumatic actuators with tunable bending stiffness, tailored deformation shapes, and considerable output force based on a wearable structured skin. Unlike conventional methods, the structured skin and the elastomeric tube are here designed and assembled separately. The elastomeric tube provides the driving force when inflating, and the structured skin acts as a guide of deformation according to designed geometrical constraints. A skin can easily be replaced with a new one to generate another deformation mode. The design strategy developed here allows us to use only an air channel and diverse wearable structured skins to achieve complex deformations. Moreover, structured skins made of different structured fabrics are reusable. One can easily recycle the old skin to form a new one with different functionalities in a few minutes. These advantages make the actuator a potential candidate for soft robots, that is environmentally and economically durable. The size and arrangement of unit cells in the structured skin lead to different bending or stretching deformation modes. The bending angle and the output force were investigated experimentally and numerically. In addition, we further extended the soft actuators to construct a soft gripper that can locate, grasp, lift, and move items with a wide range of shape, stiffness, and weight. This work opens up an avenue for designing reusable pneumatic soft robots with multiple deformation modes and abilities.

4. Experimental Section

Fabrication of the Elastic Pneumatic Actuator. The elastic pneumatic actuator comprised an elastic tube and an attached structured skin. The tube featured a diameter of 18 mm, a thickness of 3 mm, and a length of 120 mm (Figure S4Bi, Supporting Information). It was fabricated by pouring Ecoflex silica gel (SMOOTH-ON) in a mold and cured. As a pneumatic channel, the elastic tube had good air tightness and expansion performance. The structured skin was fabricated by stitching two pieces of 3D-printed structured fabric with equal numbers of rows $m = 13$ and a constant strut diameter $d = 0.5$ mm. Here, the total number of columns of the structured fabrics was 12. The structured fabric was manufactured by selective laser sintering using a 3D printer (EOS SLS system P396) with Nylon as the base material (Figure S4B ii, Supporting Information). The elastic tube was bonded with an inflation plug connected to an air tube to form a closed pipe (Figure S4A, Supporting Information). A 5.5 mm-thick annular space was reserved on the inflation plug to install the direction knob. The direction knob was composed of two semicircular knobs with a thickness of 5 mm (Figure S4A, Supporting Information). After inserting the inflation plug, it could drive the skin to rotate freely around the inflation plug, change the wearing angle of the structured skin, and then change the bending direction of the actuator. Holes were reserved on each semicircular knob to facilitate the stitching of the structured skin to the assembled direction knob. The lower end of the structured skin was similarly connected with a circular end cover (Figure S4A, Supporting Information). This stitching connection dramatically reduced the difficulty of installation and made it possible to replace and reuse the structured skin. The inflation plug and the direction knob were made of photosensitive resin using low-force stereolithography (LFS) technology.

Three-Point Bending Experiment: The actuator sample was placed between an indenter and two fulcrums with a span of 70 mm, as shown in Figure 2C. Before testing, the air pressure was set to a fixed value. A vertical compression load was applied via the indenter on the sample. The total length of the tested actuator was 125 mm, of which the effective length was 100 mm, and the cross-section area was 21 mm (the maximum section diameter could reach 32 mm after inflation). A MARK-10 tensile tester was used to extract reacting forces. The dynamometer dropped at a speed of 5 mm min^{-1} , with a maximum displacement of 5 mm.

Finite-Element Analysis: To understand better the underlying deformation mechanism of the structured fabric and the skin, we built a series of numerical models using the commercial software package Abaqus/explicit.

For the structured fabric model, the rod diameter d was 0.5 mm. The unit cell lengths of octahedra in structures A and B were $l_A = 8$ mm and $l_B = 6.5$ mm, respectively. The numbers of rows and columns for each part were 8 and 2, respectively. The attached flat plate at each end featured a dimension of $6 \text{ mm} \times 6 \text{ mm} \times 50 \text{ mm}$. A hole with a diameter of 2 mm was at the center of the plate for applying the tension force, as shown in Figure S2A, Supporting Information. Since material nonlinearity had little effect on the structured fabrics, the constituent material Nylon was modeled as an isotropic linear material with Young's modulus 1.7 GPa, Poisson's ratio 0.35, and density 930 kg/m^3 . In the Step module, the Nlgeom function enabled the large deformation option. To ensure calculation accuracy, the numerical model was meshed with 35 515 quadratic tetrahedral elements (type C3D8M). A force of 10 N was applied to the hole to extract the deformation frame and the bending angle.

To reduce the calculation expense, we partially neglected the undeformed attached structures, such as the inflation plug, and used the elastic tube and the structured skin to model the elastic actuator, as shown in Figure S2, Supporting Information. The tube featured a diameter of 18 mm, a thickness of 3 mm, and a length of 120 mm. For the constitutive material, the elastic modulus was about 0.002 GPa, Poisson's ratio was nearly 0.48, and the density was about 1062 kg/m^3 . Similar to the structured fabrics mentioned above, the tubular structured skin was modeled with similar geometrical configurations and the same base material. The only difference was that the numbers of rows and columns for each part were 13 and 6, respectively. To ensure computation accuracy, we employed meshes with 236 236 membrane elements (type M3D4) for the silicone tube and 290 011 quadratic tetrahedral elements (type C3D8M) for the structured skin. Self-contact with a friction coefficient of 0.1 was defined within the actuator. To eliminate the rigid body displacement of the tube and the skin, we applied a fixed constraint on their upper surfaces (see Figure S3C, Supporting Information). The elastic tube model was inflated with the air pressure gradually increasing from 0 to 100 kPa through the fluid cavity.

Force and Bending Angle Measurement: A bending test and an output force test were carried out to obtain the bending angle and the tip force of the proposed pneumatic actuator under different air pressure excitations. The experimental device shown in Figure S3A, Supporting Information, was used to measure the bending angle of the actuator, in which the black and white background was convenient for observing the bending of the actuator. The inflation plug was fixed on the bracket. After inflation, the angle between the normal to the actuator in the initial state and after deformation was chosen as the bending angle θ . We also established an experimental platform for measurement of the output force (see Figure S3B, Supporting Information). For the tested actuator, the upper end was fixed on the base, whereas the lower end was in direct contact with the dynamometer. After the air pressure was adjusted, the actuator bent and generated a thrust on the dynamometer, thus allowing measurement of the output force.

Supporting Information

Supporting Information is available from the Wiley Online Library or from the author.

Acknowledgements

This work was supported by the National Nature Science Foundation of China under grant no. 12202118, the MTC IRG award (M21K2c0118), and AME YIRG award (A2084c0162), both funded by Singapore Agency for Science, Technology and Research (A*STAR). W.G. also gratefully acknowledges financial support from China Scholarship Council (CSC202106120089), Heilongjiang Touyan Team (HITTY-20190003), Young Elite Scientist Sponsorship Program by Heilongjiang Province (2022QNTJ0015), and Heilongjiang Province Postdoctoral Fund (LBH-Z22105).

Conflict of Interest

The authors declare no conflict of interest.

Data Availability Statement

The data that support the findings of this study are available from the corresponding author upon reasonable request.

Keywords

pneumatic actuation, reusable robots, soft actuator, structured fabrics, variable stiffness

Received: May 30, 2023
Revised: September 7, 2023
Published online:

-
- [1] D. Rus, M. T. Tolley, *Nature* **2015**, 521, 467.
[2] C. Laschi, B. Mazzolai, M. Cianchetti, *Sci. rob.* **2016**, 1, eaah3690.
[3] J. W. Booth, D. Shah, J. C. Case, E. L. White, M. C. Yuen, O. Cyr-Choiniere, R. Kramer-Bottiglio, *Sci. Rob.* **2018**, 3, eaat1853.
[4] W.-K. Lee, D. J. Preston, M. P. Nemitz, A. Nagarkar, A. K. MacKeith, B. Gorissen, N. Vasios, Versus. Sanchez, K. Bertoldi, L. Mahadevan, G. M. Whitesides, *Sci. Rob.* **2022**, 7, eabg5812.
[5] R. F. Shepherd, F. Ilievski, W. Choi, S. A. Morin, A. A. Stokes, A. D. Mazzeo, X. Chen, M. Wang, G. M. Whitesides, *Proc. Natl. Acad. Sci. USA* **2011**, 108, 20400.
[6] H. Wang, M. Totaro, L. Beccai, *Adv. Sci.* **2018**, 5, 1800541.
[7] H.-L. Park, Y. Lee, N. Kim, D.-G. Seo, G.-T. Go, T.-W. Lee, *Adv. Mater.* **2020**, 32, 1903558.

- [8] X.-Q. Wang, K. H. Chan, Y. Cheng, T. Ding, T. Li, S. Achavananthadith, S. Ahmet, J. S. Ho, G. W. Ho, *Adv. Mater.* **2020**, 32, 2000351.
[9] E. W. Hawkes, L. H. Blumenschein, J. D. Greer, A. M. Okamura, *Sci. Rob.* **2017**, 2, eaan3028.
[10] R. Deimel, O. Brock, *Int. J. Rob. Res.* **2016**, 35, 161.
[11] M. A. Robertson, J. Paik, *Sci. Rob.* **2017**, 2, eaan6357.
[12] R. V. Martinez, J. L. Branch, C. R. Fish, L. Jin, R. F. Shepherd, R. M. Nunes, Z. Suo, G. M. Whitesides, *Adv. Mater.* **2013**, 25, 205.
[13] Q. Ji, J. Moughames, X. Chen, G. Fang, J. J. Huaroto, V. Laude, J. A. I. Martnez, G. Ulliac, C. Clévy, P. Lutz, K. Rabenoroosa, V. Guelpa, A. Spangenberg, J. Liang, A. Mosset, M. Kadic, *Commun. Mater.* **2021**, 2, 93.
[14] C. Coulais, A. Sabbadini, F. Vink, M. van Hecke, *Nature* **2018**, 561, 512.
[15] M. Brandenbourger, C. Scheibner, J. Veenstra, V. Vitelli, C. Coulais, arXiv preprint arXiv:2108.08837, **2021**.
[16] M. Manti, T. Hassan, G. Passetti, N. D'Elia, C. Laschi, M. Cianchetti, *Soft Rob.* **2015**, 2, 107.
[17] M. C. Yuen, R. A. Bilodeau, R. K. Kramer, *IEEE Rob. Autom. Lett.* **2016**, 1, 708.
[18] G. Haghighashtiani, E. Habtour, S.-H. Park, F. Gardea, M. C. McAlpine, *Extreme Mech. Lett.* **2018**, 21, 1.
[19] A. Miriyev, K. Stack, H. Lipson, *Nature Commun.* **2017**, 8, 596.
[20] L. Jin, A. E. Forte, B. Deng, A. Rafsanjani, K. Bertoldi, *Adv. Mater.* **2020**, 32, 2001863.
[21] E. Siéfert, E. Reyssat, J. Bico, B. Roman, *Nature Mater.* **2019**, 18, 24.
[22] Q. Guan, J. Sun, Y. Liu, N. M. Wereley, J. Leng, *Soft Rob.* **2020**, 7, 597.
[23] H. K. Yap, H. Y. Ng, C.-H. Yeow, *Soft Rob.* **2016**, 3, 144.
[24] J. Yan, X. Zhang, B. Xu, J. Zhao, *Soft Rob.* **2018**, 5, 527.
[25] J. Yi, X. Chen, C. Song, Z. Wang, *Soft Rob.* **2018**, 5, 81.
[26] J. Wirekoh, Y.-L. Park, *Smart Mater. Struct.* **2017**, 26, 035009.
[27] F. Daerden, D. Lefeber, *Int. J. Fluid Power* **2001**, 2, 41.
[28] L. A. Al Abeach, S. Nefti-Meziani, S. Davis, *Soft Rob.* **2017**, 4, 274.
[29] X. Chen, L. W. Taylor, L.-J. Tsai, *Textile Res. J.* **2011**, 81, 932.
[30] J. Engel, C. Liu, *J. Micromech. Microeng.* **2007**, 17, 551.
[31] Y. Wang, L. Li, D. Hofmann, J. E. Andrade, C. Daraio, *Nature* **2021**, 596, 238.
[32] J. Pardomuan, N. Takahashi, H. Koike, *IEEE Access* **2022**, 10, 80495.
[33] A. R. Ploszajski, R. Jackson, M. Ransley, M. Miodownik, *MRS Adv.* **2019**, 4, 1361.
[34] C. Coulais, E. Teomy, K. De Reus, Y. Shokef, M. Van Hecke, *Nature* **2016**, 535, 529.
[35] X. Tan, Y. Li, L. Wang, K. Yao, Q. Ji, B. Wang, V. Laude, M. Kadic, *Adv. Intelligent Sys.* **2023**, 5, 2200400.
[36] Y. Fei, J. Wang, W. Pang, *Soft Rob.* **2019**, 6, 1.